Biomass and Bioenergy 194 (2025) 107633

Contents lists available at ScienceDirect

Biomass and Bioenergy

journal homepage: www.elsevier.com/locate/biombioe

# Scalable synthesis of heteroatom-doped carbons from waste hemp hurd with enhanced sodium-ion and potassium-ion storage capabilities

Daniel Antorán [a,b], Darío Alvira [a,b], Víctor Sebastián [b,c,d], Joan J. Manyà [a,b,*]

[a] Aragón Institute for Engineering Research (I3A), Thermochemical Processes Group, University of Zaragoza, Escuela Politécnica Superior, Crta. de Cuarte s/n, 22071, Huesca, Spain
[b] Department of Chemical Engineering and Environmental Technologies, University of Zaragoza, Campus Río Ebro, María de Luna 3, 50018, Zaragoza, Spain
[c] Instituto de Nanociencia y Materiales de Aragon (INMA), CSIC-University of Zaragoza, Campus Río Ebro, Edificio I+D, Mariano Esquillor s/n, 50018, Zaragoza, Spain
[d] Networking Research Center on Bioengineering, Biomaterials and Nanomedicine, CIBER-BBN, 28029, Madrid, Spain

ARTICLE INFO

*Keywords:*
Sodium-ion batteries
Potassium-ion batteries
Hard carbon
Waste hemp hurd
Heteroatom doping
Hydrothermal pretreatment

ABSTRACT

In this study, we applied an easily scalable two-step process comprising hydrothermal pretreatment with simultaneous mild heteroatom doping (N, N-S, and N-P) followed by carbonization at 800 °C to synthesize hard carbons (HCs) from waste hemp hurd for Na-ion and K-ion storage. The proposed synthesis pathway represents a viable alternative to the more energy-intensive, environmentally harmful, and/or challenging to scale up processes reported in the literature. The resulting carbons, particularly the dual NP-doped and single N-doped varieties, demonstrated improved electrochemical performance in terms of specific capacity (indicating more reversible ion storage sites) and rate capability (reflecting faster ion transport kinetics). These enhancements can be attributed to structural and surface chemistry modifications introduced during hydrothermal pretreatment. For Na-ion storage, the N-doped HC achieved a specific capacity of 293.6 mAh $g^{-1}$ at 0.1 A $g^{-1}$ (and 125 mAh $g^{-1}$ at 1 A $g^{-1}$) with an initial coulombic efficiency (ICE) of 73.5 % using an ester-based electrolyte. The same material showed an enhanced rate capability when an ether-based electrolyte was employed, achieving 155 mAh $g^{-1}$ at 1 A $g^{-1}$. For K-ion half-cells, the dual N-P-doped HC exhibited the best performance at low current rates, delivering a specific capacity of 260 mAh $g^{-1}$ at 0.1 A $g^{-1}$ in ester-based electrolytes. However, the N-doped HC showed the best rate capability at 2 A $g^{-1}$ (57 mAh $g^{-1}$), which is a reasonable value given the lack of mesopores in produced HCs.

## 1. Introduction

Rechargeable lithium-ion batteries (LIBs) currently represent the state-of-the-art electrochemical energy storage (EES) systems owing to their high energy density and long cycle-life. However, due to the increasing deployment of renewable energy sources, an unprecedented expansion of the globally installed energy storage capacity is required. In this context, promising post-lithium technologies based on replacing lithium with cheaper and more widely available alkali metal species, such as sodium and potassium, have been explored in the last years. Nevertheless, much research efforts are still needed to develop sustainable and high-performance electrode materials for post-lithium EES systems [1].

In sodium-ion batteries (SIBs), graphite, which is commonly used as anode (i.e., negative electrode) in LIBs, exhibits significantly limited sodium-ion storage capacity (approximately 35 mAh $g^{-1}$) when carbonate-based electrolytes are employed. In potassium-ion batteries (PIBs), the insertion and extraction of potassium-ions with a larger radius (1.38 Å) induces significant volumetric expansion changes in the graphite electrodes during cycling, leading to limited cycling stability [2]. To advance the scalability of SIBs and PIBs, improvements are needed across various components of the cell, with a particular focus on enhancing electrode performance and improving the ion conductivity and stability of the solid electrolyte interphase (SEI). Additionally, electrodes should be manufactured from sustainable raw materials using energy-efficient and environmentally friendly production processes [3].

To date, substantial efforts have been made in the synthesis of alternative advanced carbon-based materials to be used as anodes in

* Corresponding author. Aragón Institute for Engineering Research (I3A), Thermochemical Processes Group, University of Zaragoza, Escuela Politécnica Superior, Crta. de Cuarte s/n, 22071, Huesca, Spain.
*E-mail address:* joanjoma@unizar.es (J.J. Manyà).

https://doi.org/10.1016/j.biombioe.2025.107633
Received 22 November 2024; Received in revised form 16 January 2025; Accepted 16 January 2025

SIBs and, to a lesser extent, in PIBs. Hard carbons (HCs) derived from biomass sources, which are low-cost and renewable alternatives to fossil-based carbon materials, are attractive candidates for both SIB and PIB purposes due to their high electrical conductivity and chemical stability [4–6]. HCs are usually composed of randomly oriented turbostratic graphene nanosheets with an expanded interlayer spacing ($d_{002}$) and relatively abundant open/closed nanopores. These structural features can facilitate ion and electron transport, leading to appropriate storage capacities, even at relatively high current rates.

Storage of $Na^+$ ions into HCs primarily occurs in two main stages during galvanostatic discharge: (1) a sloping region at relatively high voltages (above 0.15 V vs. $Na^+$/Na), where storage of sodium ions is mainly attributed to adsorption processes driven by surface charge storage, heteroatoms, and defects; and (2) a plateau region at lower voltages (below 0.15 V vs. $Na^+$/Na), which is mainly associated with intercalation and pore filling processes [7]. For potassium ion storage, galvanostatic discharge profiles can also be divided into two parts: (1) a high potential region (above 0.5 V vs. $K^+$/K) associated to adsorption processes; and (2) a low potential region (below 0.5 V vs. $K^+$/K), where intercalation is the dominant $K^+$-ion storage process [8]. Nonetheless, biomass-derived HCs anodes still exhibit certain limitations that hinder their implementation at large scale, such as low initial coulombic efficiency (ICE) [9,10] and poor cycling stability in comparison with graphite-based anodes in LIBs [11,12]. To overcome these issues, a better understanding of the complex phenomena occurring at the electrode-electrolyte interphase is essential for fine-tuning the properties of HCs, especially in terms of pore size distribution and functional groups on surface. In this sense, hierarchical pore size distributions (with appropriate volumes of both micro- and mesopores) can lead to an improved storage capacity and rate capability [13], but they can also result in extremely low ICE values depending on the electrolyte formulation.

In addition to the possibility of tailoring the inherent material features of HCs, the introduction of heteroatoms (like N, P, S, etc.) into their structure is a well-known strategy to further enhance their electronic/ion conductivity and introducing functional groups on surface that may boost electrochemical storage properties [14–17]. Co-doping appears as a very promising approach to improve the overall performance of the resulting carbon materials due to a synergetic effect. For instance, co-doping with N and P can lead to enhanced structural distortion and larger interlayer spacing, which is especially beneficial for the reversible adsorption/intercalation of $K^+$ ions [18]. On the other hand, previous studies reported the synergistic effect of co-doping with N and S, which not only can promote the electronegativity of carbon and thereby enhancing the absorption of $Na^+$ ions, but also can induce additional modifications in the surface and structural properties of carbons, resulting in an enhanced sodium storage performance [19,20]. Furthermore, the versatility of heteroatom-doped carbons extends beyond energy storage to other applications, such as environmental remediation [21], and heterogenous catalysis [22]. For example, biomass-derived carbons functionalized with metal oxides have been successfully employed for heavy metal adsorption [23].

In recent years, industrial hemp (*cannabis sativa L.*) production in the EU has increased significantly, from 20,540 ha in 2015 to 33,020 ha in 2022 [24]. Industrial hemp fiber is considered by the European Commission as a sustainable raw material for both the textile and paper industry. However, hemp hurd (the inner lignocellulosic portion of hemp stalk) is the by-product of the hemp defibration process and it is most often discarded together with the leaves. Therefore, there is a strong need for the development of technology to valorize waste hemp hurd (WHH) sourced from industrial hemp into renewable value-added biomaterials [25].

In recent years, there has been a growing interest in using WHH as a precursor for carbon materials in EES devices (see Fig. S1 in Supporting Information). For instance, Wang et al. produced N-doped high specific surface area carbon nanosheets (840 $m^2\ g^{-1}$) from hemp fibers via hydrothermal pretreatment, activation with KOH at 850 °C, and hydrothermal posttreatment with urea [26]. When the synthesized carbons were tested as anodes in sodium-ion half-cells, they exhibited an impressive capacity of 173 mAh $g^{-1}$ at 1 A $g^{-1}$, but a very low ICE (43 %). More recently, a notable rate capability for a sodium-ion half-cell (79 mAh $g^{-1}$ at 1 A $g^{-1}$) was also reported in our previous study for WHH-derived HCs produced through mild chemical activation with $K_2CO_3$ [27]. The electrochemical performance of WHH-derived HCs for sodium-ion storage was notably improved via an easily scalable process involving hydrothermal pretreatment assisted by HCl and subsequent annealing at 1000 °C [28]. The resulting carbon-based anodes delivered specific capacities of 535 and 115 mAh $g^{-1}$ at current densities of 0.03 and 1 A $g^{-1}$, respectively. In the context of PIBs, Wang et al. produced fluorine-doped carbon electrodes derived from industrial hemp core and using PTFE as fluoride agent [29]. The resulting carbons showed an excellent rate capability (369.6 and 229.3 mAh $g^{-1}$ at 0.2 and 2 A $g^{-1}$, respectively).

With all the above kept in mind, the specific aim of the present study was to synthesize single N-doped and dual N-P- and N-S-doped hard carbons from WHH as a precursor, sourced from Narlisaray in the Black Sea region of Turkey. The synthesis was conducted through a two-step easily scalable process comprised of a hydrothermal pretreatment followed by carbonization at a moderate-higher temperature of 800 °C. Unlike most previous studies, which often focus exclusively on either sodium- or potassium-ion batteries and rarely compare the impact of different electrolyte formulations, this work systematically evaluates the storage capabilities of both $Na^+$ and $K^+$ ions across multiple configurations. It provides valuable insights into the complex interactions at the electrode-electrolyte interface and assesses the potential of doped carbons to address key challenges in post-lithium energy storage technologies. Additionally, this study integrates sustainability, scalability, and versatility to advance the understanding of biomass-derived carbons and contribute to the development of practical and efficient energy storage solutions.

## 2. Experimental section

### 2.1. Synthesis of hard carbons

The WHH samples used here were characterized in detail through proximate and elemental analyses, as well as determination of the main biomass constituents (extractives, hemicellulose, cellulose, and lignin) and the main species present in ash. More details on the analytical methods adopted are given elsewhere [27].

Doped hard carbons were synthesized via a two-step process: 5 g of WHH (previously sieved to particle sizes below 5 mm) and 1 g of dopant source (urea, ammonium sulphate, and ammonium dihydrogen phosphate for N, N-S, and N-P doping, respectively) were dissolved in 60 mL of DI water. The resulting mixture was subjected to hydrothermal treatment using a PTFE-lined stainless-steel autoclave (Huanyu ZHT-172C) at a highest temperature of 180 °C for 12 h. After cooling to room temperature, the resulting hydrochar (ca. 2 g per batch) was collected through vacuum filtration, dried at 100 °C for 12 h, and then carbonized at a highest temperature of 800 °C using a tubular mullite-made reactor inserted into a high-temperature furnace (Carbolite TF1 16/60/300) under a continuous flow of argon at a heating rate of 5 °C $min^{-1}$. To extract inorganics and unreacted doping agents, the resulting carbon was washed using a HCl solution (2 mol $dm^{-3}$) and then rinsed with DI water until neutral pH was achieved. The final hard carbon was dried (at 100 °C for 12 h), grounded, and sieved to collect particles below 90 μm. For comparison purposes, an undoped carbon (H800) was produced under the same thermochemical process route described above. The doped materials were designated as HN800, HNS800, and HNP800, indicating the respective dopant source (see Fig. S2 for a visual summary of the synthesis pathway).

### 2.2. Physicochemical characterization of hard carbons

To investigate the structural properties of produced carbons, X-ray diffraction (XRD) and Raman spectroscopy were employed. XRD analysis was performed using an Empyrean instrument from Malvern Panalytical (UK), with a wavelength of 0.154 nm. This technique allowed for the determination of parameters such as the graphene interlayer spacing ($d_{002}$), the apparent crystallite thickness of crystallites along the c-axis ($L_c$), the apparent width of crystallites along the a-axis ($L_a$), and the number of graphene stacking layers ($n$) through the application of Bragg's law and Scherrer's equation [30]. Raman spectroscopy was conducted using an Alpha 300 instrument from WITec (Germany) at a laser wavelength of 532 nm. The acquired Raman spectra were deconvoluted into one Gaussian-shaped band (D3) and four Lorentzian-shaped bands (G, D1, D2, and D4) using the Peak Analyzer tool in OringinPro software, following the procedure described by Sadezky et al. [31].

Morphological features of the samples were analyzed using scanning electron microscopy (SEM) and high-resolution transmission electron microscopy (HR-TEM). SEM was performed using an Inspect F50A microscope (FEI, Eindhoven, The Netherlands). A Titan microscope (FEI, Eindhoven, The Netherlands), operating at 300 kV and equipped with a SuperTwin® objective lens and a CETCOR objective corrector from CEOS Company (with a point-to-point resolution of 0.08 nm), was used for HR-TEM. Interplanar distances were determined from HR-TEM images using Digitalmicrograph™ software.

Furthermore, X-ray photoelectron spectroscopy (XPS) was used to assess the availability on surface of heteroatom-containing functional groups. XPS measurements were conducted using an Axis Supra system (Katros Analytical, UK) with a monochromatic Al Kα X-ray source (1486 eV). The relevant regions of the spectra were deconvoluted using CasaXPS software. To evaluate the narrow porosity of HCs, $CO_2$ adsorption isotherms at 0 °C were obtained using an Autosorb-iQ-XR2 analyzer (Quantachrome Instruments, Germany). From $CO_2$ adsorption data, both the specific surface area ($S_{BET}$) and volume of ultramicropores (pore size less than 0.7 nm) were estimated using the Brunauer-Emmett-Teller equation and a non-local density functional theory (NLDFT) model for slit pore geometry, respectively.

### 2.3. Electrochemical performance measurements

Carbon-based electrodes were composed of (percentages in mass): 80 % WHH-derived HCs, 10 % acetylene black (as conductive agent), and 5 % styrene-butadiene rubber (SBR) and 5 % sodium carboxymethyl cellulose (Na-CMC) as co-binders. A homogenized slurry was obtained by adding DI water under vortex agitation and magnetic stirring. Then, the slurry was uniformly coated on a high-purity aluminum sheet (current collector) using a baker applicator, resulting in a composite electrode with a thickness of 100 μm. Finally, the resulting electrodes were punched into discs (12 mm diameter) and dried under vacuum at 120 °C for 12 h. The final mass loading of working electrodes was 1.53 ± 0.34 mg $cm^{-2}$.

Customized three-electrode t-type Swagelok half-cells—see Fig. S3—were assembled in an Ar-filled glovebox with $O_2$ and $H_2O$ contents below 0.5 ppm. Metallic sodium (for SIBs) or potassium (for PIBs) were used as counter electrode (12 mm diameter discs) and reference electrode (5 mm diameter discs). As separator, two 190 mm thickness glass fiber filters were used. Two different electrolyte formulations, previously tested in a prior study [32], were used for SIBs with a fixed volume of 120 μL: (a) 1 mol $dm^{-3}$ NaTFSI in a mixture (1:1 in volume) of dimethyl carbonate (DMC) and ethylene carbonate (EC), and (b) 1 mol $dm^{-3}$ $NaPF_6$ in diglyme (DGM). For KIBs, the electrolyte formulations (120 μL) used were: (a) 0.8 mol $dm^{-3}$ $KPF_6$ in a mixture (1:1 in mass) of DMC and EC, and (b) 1 mol $dm^{-3}$ KFSI in a mixture (1:1 in mass) of diethyl carbonate (DEC) and EC.

All the electrochemical measurements were conducted using a potentiostat-galvanostat (model SP-200 from Bio-Logic, France) at room temperature. Galvanostatic discharge/charge (GCD) measurements were carried out within a potential window of 0.01–2.5 V (vs. $Na^+/Na$), and 0.01–3.0 V (vs. $K^+/K$), whereas cyclic voltammetry (CV) curves were obtained at a scan rate of 0.1 mV $s^{-1}$ within the same voltage windows. Galvanostatic intermittent titration technique (GITT) measurements were also conducted at a constant current density of 0.03 A $g^{-1}$, a pulse time of 20 min, and relaxation periods of 1 h at open circuit. The working electrodes were previously subjected to three CV scans to allow the formation and stabilization of the SEI layer.

## 3. Results and discussion

### 3.1. Material features

Table S1 (SI) reports the results obtained from raw WHH characterization. The relatively well-balanced contents of hemicellulose, cellulose, and lignin (38.1 %, 32.0 %, and 23.8 %, respectively, in weight basis), could be interesting for sodium- and potassium-ion storage purposes. As recently reported by Liao et al. [33], relatively high contents of cellulose could result in smaller and randomly oriented pseudographitic layers as well as closed pores (depending on the highest annealing temperature), which contribute to high reversible storage capacity; while precursors with relatively high lignin contents usually results in mostly open porous structures, which favor ion diffusion and cycling stability.

Fig. 1 illustrates SEM images of the HCs synthesized in this study. From all the images, it can be seen that all the produced HCs retain the characteristic structures of the original biomass, including fibers, pores, and channels. The samples also exhibited a considerably rough surface and the presence of some microspheres attached to the main structure. These features can be ascribed to the hydrothermal pretreatment, which promotes hydrolysis of cellulose and hemicellulose to soluble monomers and the subsequent polymerization and condensation of them to form carbon microspheres [34]. However, the sizes and availability of microspheres differed significantly depending on the doping agent used, with diameters ranging from 0.33 μm (Fig. 1b) to 10 μm (Fig. 1d) for HNP800 and HNS800, respectively. When urea was used as N-doping agent, the formation of agglomerated microspheres was promoted (see Fig. 1c). This phenomenon could be attributed to reactions between carbonyl groups on the surface of nascent hydrochar and the amino groups in urea, leading to the formation of hydroxymethyl-containing compounds, which subsequently condense into microspheres [35].

Fig. 2 displays selected HR-TEM images of HCs. Overall, mostly amorphous structures with randomly distributed pseudographitic domains were observed in all cases. According to the literature, interlayer spacing values of 0.37–0.40 nm for sodium ion [36] and around 0.38 nm for potassium ion [37] can optimize the intercalation of these ions in carbonaceous materials. Such spacings can also contribute to buffer the volume change during the fast insertion–extraction process of ions [38]. As depicted in Fig. 2b, the HN800 material showed local domains with considerably expanded interlayer distances (i.e., above 0.4 nm), whereas HNP800 (Fig. 2e) and HNS800 (Fig. 2f) exhibited relatively narrow interlayer spacing (i.e., below 0.37 nm) with certain highly ordered domains with planar distances below 0.30 nm. Interestingly, urea doping also resulted in the formation of highly ordered local domains during the carbonization process, as shown in Fig. 2c, where well defined fully graphitic 2D structures are visible. Furthermore, the co-existence of both disordered and ordered domains in HN800 is clearly evident in Fig. 2d.

Regarding the results from XRD analysis, Fig. 3a displays the patterns obtained for hard carbons. As expected, two board peaks were identified, with approximate centers at 23° and 44°. The first peak correlates with the spacing between graphene layers, whereas the second peak is primarily linked to the contributions of the (100) and (101) reflections [5]. Table 1 reports the calculated parameters using the Bragg's law and the Scherrer's equation. Despite the apparent differences in interlayer

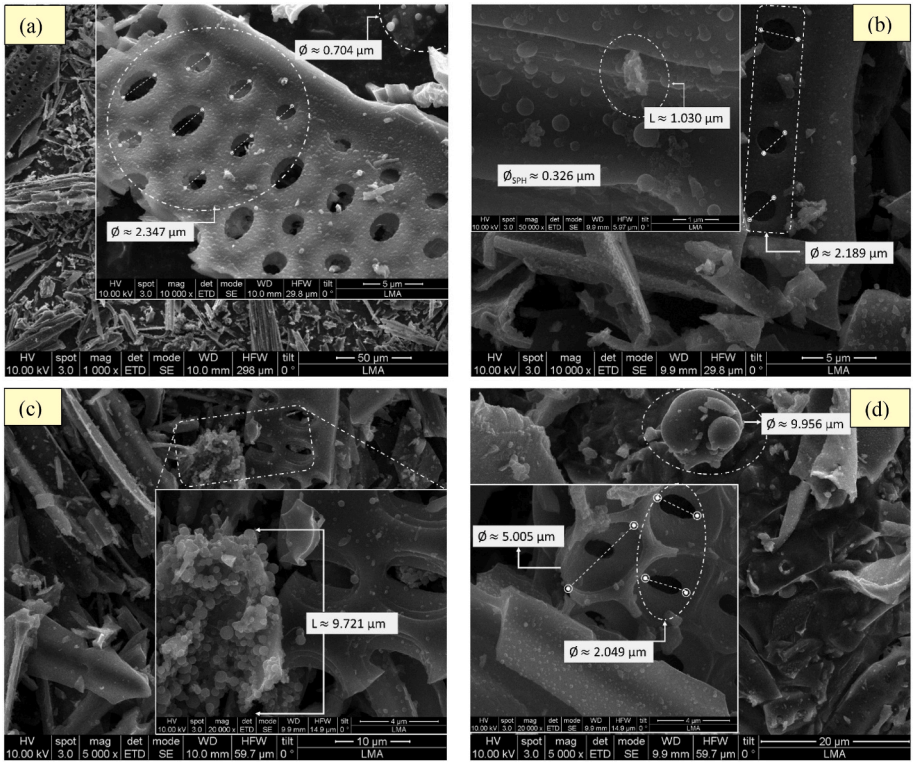


**Fig. 1.** SEM images of WHH-derived carbons: H800 (a), HNP800 (b), HN800 (c), and HNS800 (d).

spacing values for local domains deduced from the HR-TEM images shown in Fig. 2, $d_{002}$ values for bulk HCs reported in Table 1 were quite similar (within the range of 0.37–0.39 nm). After analyzing the rest of structural parameters listed in Table 1 (including those deduced from Raman spectra given in Figs. S4a and S4b), no significant differences were observed regarding the degree of disorder. Probably HNS800 could have a slightly more disordered structure, given the values obtained for $A_{D1}/A_G$ and $L_a$. This may be explained by the fact that the hydrothermal treatment itself already favored the introduction of numerous structural defects by, for instance, intrinsic carbon dislocation and vacancies and oxygen doping [39].

Table 2 reports the elemental composition found on the surface of WHH-derived hydrochar (obtained using DI water as hydrothermal medium) and WHH-derived HCs, which was determined from the acquired survey XPS spectra (see Figs. S5–S9). Only K and Si from the raw biomass were detected in the WHH-derived carbons. As expected, the oxygen content in the resulting HCs was considerably lower than that obtained for hydrochar (33.9 %), which was relatively high as a consequence of the introduction of oxygen-containing functional groups during hydrothermal carbonization. Interestingly, heteroatom-doped HCs exhibited higher oxygen contents with respect to the undoped H800 carbon. Abundant oxygen groups can increase electrode surface wettability and also provide extra pseudocapacitive active sites. From Tables 2 and it can also be observed that the atomic contents on surface of dopant elements are relatively low, particularly for phosphorous and sulfur in the HNP800 and HNS800 doped carbon, respectively. Previous studies have reported atomic contents of at least 2.5 % for S-doped carbons [40] and 1.1 % for P-doped carbons [41]. These findings suggest that the chemical agents employed in this work for S- and P-doping resulted in modest yields of heteroatom incorporation into the carbon structure.

The high-resolution spectra of C 1s region were deconvoluted into six peaks, corresponding to C—C bonds associated with aromatic $sp^2$ carbons (281.8–282.0 eV), C—C bonds linked to $sp^3$ carbons and defective carbon structures (282.7–283.6 eV), defective carbons and C—O groups (284.2–284.4 eV), C═O groups (287.3–287.4 eV), O═C—O groups (290.1–290.2 eV), and π—π* transitions (292.2–293.3 eV) [42,43]. Similarly, the deconvoluted high-resolution spectra of O 1s region revealed four peaks corresponding to C═O bonds in quinones (529.3–529.5 eV), C—O bonds in hydroxyl and phenolic groups (530.3–530.4 eV), C—O bonds in esters and anhydrides groups, as well as C═O bonds in carboxylic groups (531.1–532.7 eV), and adsorbed moisture and oxygen (534.1–534.8 eV) [44]. Additionally, the high-resolution scan of the N 1s region was deconvoluted into pyridinic N (395.5–395.7 eV), pyrrolic N (398.1–398.3 eV), and quaternary N (400.1–400.4 eV).

Results from deconvolution are graphically summarized in Fig. 3b–d. The doped HCs showed a higher proportion of aromatic $sp^2$ C—C bonds, attributed to the introduction of heteroatoms and the subsequent formation of more conjugated structures. From deconvolution of O 1s regions, it can also be observed that HNP800 and HN800 featured a higher content of C═O bonds (see Fig. 3c), which promote reversible adsorption of both $Na^+$- and $K^+$-ions, thereby increasing the storage capacity of the HC-based anode [43,45]. Additionally, deconvolution results of N 1s regions indicated a marked increase in pyridinic N, at the expense of quaternary N, when extrinsic doping agents were used (see Fig. 3d). It is generally assumed that both pyrrolic (the most abundant N configuration for synthesized HCs) and pyridinic N are more effective for electrochemical energy storage. In this context, Feng et al. reported that pyrrolic N has a more suitable $Na^+$-ion adsorption energy [46], whereas Xie et al. corroborated that high contents of pyridinic N favored the creation of additional active sites for reversible adsorption of $K^+$ ions [47]. Deconvolution of S 2p region for the HNS800 material led to two peaks at the binding energies of ca. 163.4 eV (S 2p3/2) and ca. 164.4 eV (S 2p1/2), representing C—S—C covalent bonds (see Fig. S9). For the dual N-P-doped HC, the limited signal in the P 2p region prevented an accurate deconvolution (see Fig. S7).

Table 2 also lists the specific surface areas ($S_{BET}$) deduced from $CO_2$ adsorption isotherms (which are shown in Fig. S10). Similar $S_{BET}$ values and narrow micropore (i.e., below 1 nm) size distributions (see also

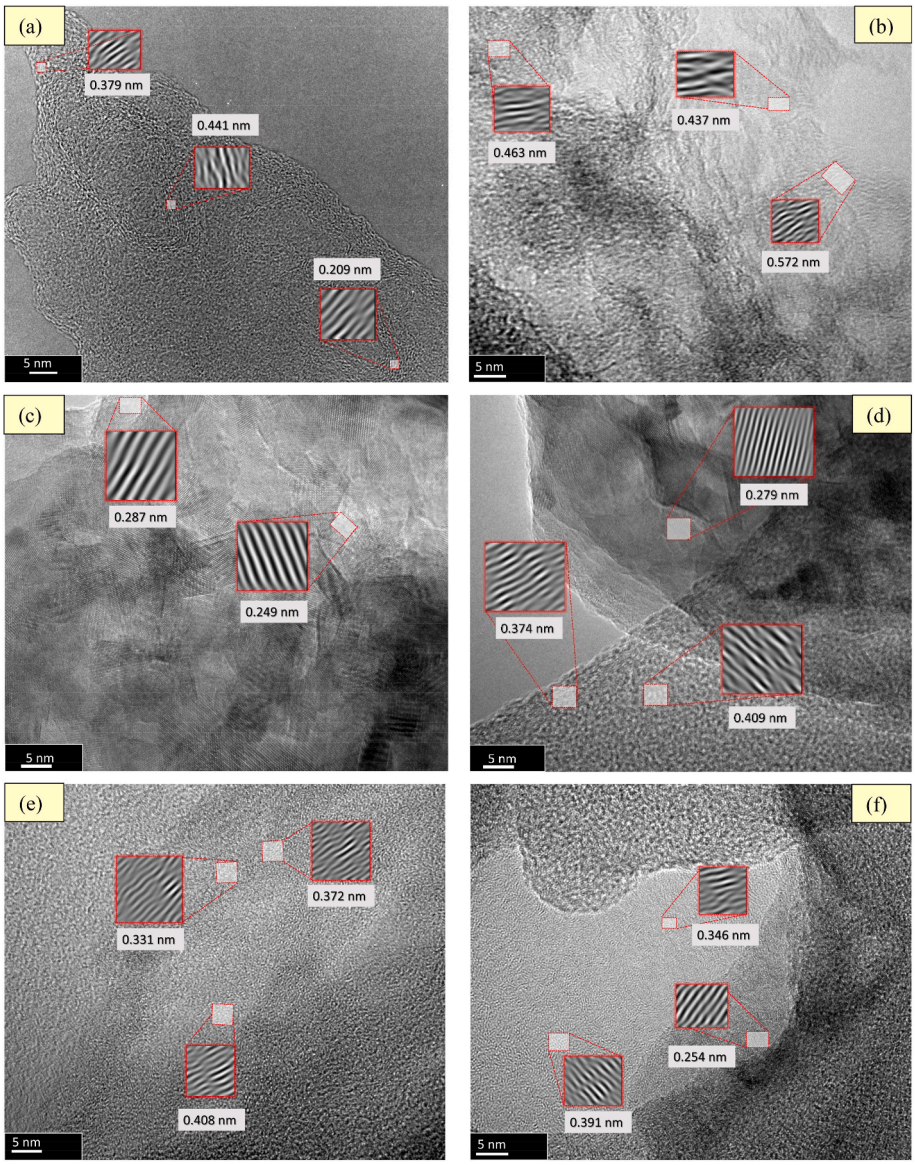


**Fig. 2.** HR-TEM images of H800 (a), HN800 (b–d), HN800 (d), and HNS800 (e).

Fig. S11) were obtained for all the produced HCs. Moderate microporous surface areas, like those reported in the present stuy, could lead to reasonable ICE values (i.e., above 70 %) without compromising the diffusion rate of ions through the electrode [27,48–50]. In addition, the bimodal pore size distributions of HCs, with peaks at ca. 0.35 nm and 0.5 nm, indicate a dominat ultramicropore network, which could enhance the plateau capacity via pore filling and provide relatively fast transport channels for ions while simultaneously hindering the electrolyte contact with the inner surface.

### 3.2. Electrochemical performance of hard carbon-based anodes

The cyclic voltammetry curves corresponding to the first three discharge-charge cycles for H800, HNP800, HN800 and HNS800 materials are shown in Figs. 4 and 5 for sodium-ion and potassium-ion half-cells, respectively. For $Na^+$-ion half-cells, NaTFSI in DMC:EC electrolyte was used, whereas $KPF_6$ in DMC:EC (to avoid salt precipitation [50]) was the electrolyte formulation for $K^+$-ion half-cells.

In Fig. 4, the irreversible broad peak observed during the first discharge is attributed to the decomposition of the electrolyte and the subsequent formation of the SEI layer, as well as the irreversible adsorption of $Na^+$ ions in structural defects and surface functional groups. The irreversible peak observed for the undoped H800 material was more prominent in comparison with those observed for doped HCs. This could be explained by a higher extent of irreversible adsorption processes on, for instance, C—O functional groups. Furthermore, the reversible peaks appearing around 0.01 V (cathodic) and 0.15–0.20 V (anodic) are ascribed to the reversible storage and release of $Na^+$ ions in the carbon framework, respectively [51–53]. These peaks were considerably more pronounced for heteroatom-doped HCs, especially for HNP800 and HN800. As can be seen in Fig. 4d, the HNS800 material exhibited a certain instability (i.e., capacity loss between the second and third cycles), which could be attributed to irreversible sodiation processes on certain functional groups and/or continuous growth of the SEI.

Concerning the CV curves obtained for potassium-ion half-cells (Fig. 5), it should be highlighted the unstable behavior also observed for HNS800 (see Fig. 5d). The more pronounced cathodic (at ca. 0.01 V) and anodic (within the range of 0.5–0.7 V) peaks—attributed to uptake and release of $K^+$ ions—only appeared during the first discharge, indicating a high extent of irreversible $K^+$-ion storage processes. In addition, and in agreement with the findings by Qian et al., sulfur can also catalyze the reduction and decomposition of the electrolyte ($KPF_6$ in carbonate-

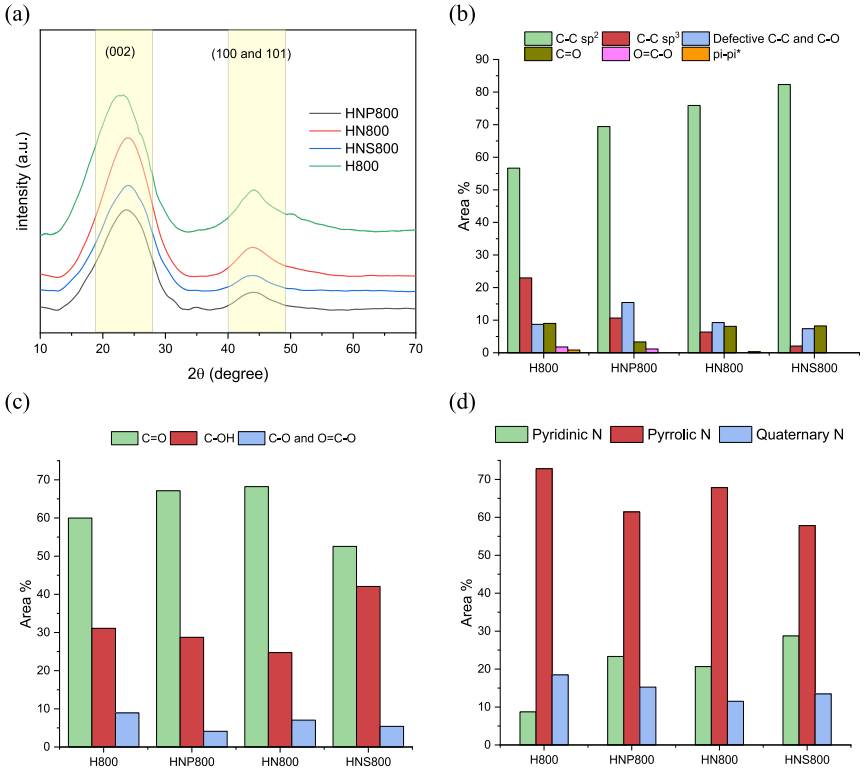


**Fig. 3.** XRD patterns of WHH-derived carbons (a), contributions (area %) of the different peaks from deconvoluted C 1s (b), O 1s (c), and N 1s (d) binding energy regions.

**Table 1**
Structural parameters of WHH-derived carbons deduced from XRD and Raman analyses.

| Material | From XRD | | | From Raman | | | |
|---|---|---|---|---|---|---|---|
| | $d_{002}$ (nm) | $L_c$ (nm) | $L_a$ (nm) | $A_{D1}/A_G$ | $L_a$ (nm) | $A_{D1}/(A_G + A_{D1} + A_{D2})$ | FWHM of D1 peak ($cm^{-1}$) |
| H800 | 0.388 | 0.895 | 3.508 | 4.79 ± 0.30 | 4.03 ± 0.24 | 0.808 ± 0.01 | 195 ± 4.77 |
| HNP800 | 0.376 | 0.899 | 2.857 | 4.44 ± 1.14 | 4.51 ± 1.06 | 0.791 ± 0.03 | 199 ± 6.75 |
| HN800 | 0.373 | 0.945 | 3.070 | 4.94 ± 0.59 | 3.93 ± 0.52 | 0.808 ± 0.02 | 202 ± 2.98 |
| HNS800 | 0.369 | 0.894 | 2.420 | 5.30 ± 0.53 | 3.65 ± 0.35 | 0.821 ± 0.01 | 205 ± 5.41 |

**Table 2**
Surface composition (at. %) obtained via integrated areas of the survey XPS spectra and specific surface areas deduced from $CO_2$ adsorption isotherms.

| Material | C | O | N | P | S | K | Si | $S_{BET}$ ($m^2\ g^{-1}$)[a] | *Ultramicropore volume* ($cm^3\ g^{-1}$)[c] |
|---|---|---|---|---|---|---|---|---|---|
| Hydrochar (in pure water) | 65.3 | 33.9 | 0.46 | ND[b] | ND | ND | 0.32 | ND | ND |
| H800 | 93.9 | 4.89 | 0.58 | ND | ND | 0.27 | 0.30 | 387.9 | 0.180 |
| HNP800 | 87.5 | 7.49 | 2.12 | 0.70 | ND | ND | 2.85 | 391.2 | 0.175 |
| HN800 | 88.1 | 7.54 | 1.32 | ND | ND | 0.16 | 2.93 | 365.8 | 0.167 |
| HNS800 | 88.7 | 6.66 | 1.82 | ND | 0.90 | ND | 2.80 | 369.1 | 0.167 |

[a] From $CO_2$ adsorption isotherm at 0 °C.
[b] Not detected.
[c] From $CO_2$ adsorption data using a NLDFT model.

based solvents) to form a thicker and more resistive SEI, resulting in a relatively poor cycling stability [54].

The different CV patterns between sodium-ion and potassium-ion half-cells could be explained by multiple reasons, including differences in binding energies of the respective ions, ionic size, etc. CV curves for $Na^+$ ion showed more pronounced peaks in the low-voltage (i.e., plateau) region, suggesting that intercalation and pore filling contributed more significantly to the overall capacity. In contrast, for $K^+$ ion, the different shape and reduced amplitude of CV peaks may suggest a dominant role of surface storage processes [18].

Fig. 6 illustrates the first five GCD cycles (at a current density of 0.1 A $g^{-1}$) for WHH-derived HCs using three-electrode sodium-ion half-cells and carbonate-based electrolyte formulations. As can clearly be seen, the incorporation of heteroatoms resulted in a higher contribution from the plateau region without compromising the slope region (see Fig. S12a). In particular, both HNP800 and HN800 doped carbons displayed remarkable electrochemical performance, with specific capacities of 270.3 and 293.6 mAh $g^{-1}$ (at 0.1 A $g^{-1}$), respectively. In addition, a remarkable ICE of 73.5 % was measured for the single N-doped carbon. The overall better electrochemical performance of HN800 could be explained by its features in terms of surface chemistry (this material exhibited the highest content of C=O bonds and pyrrolic

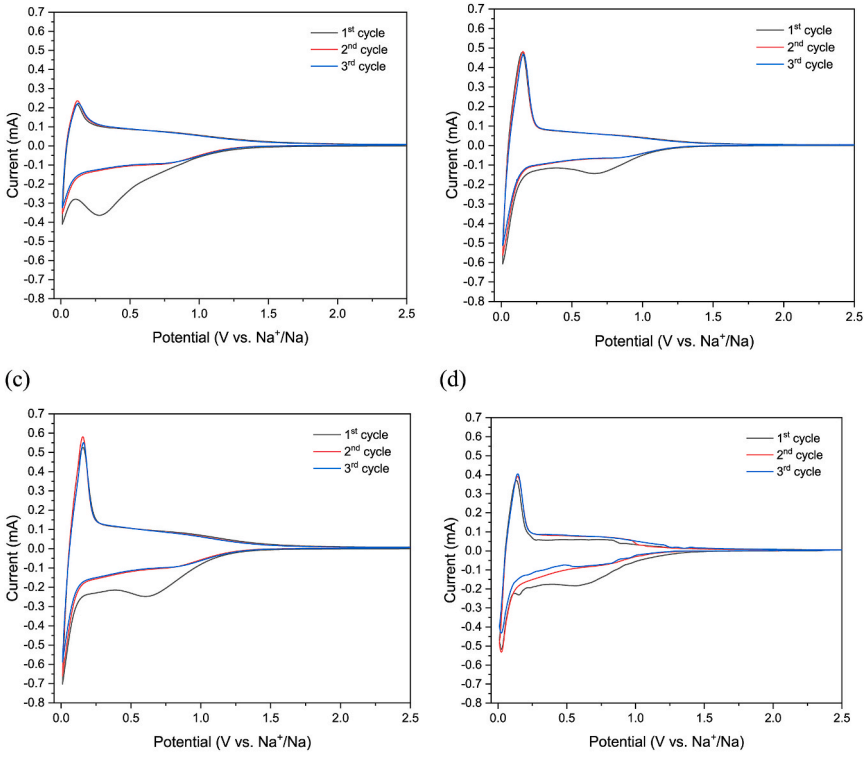


**Fig. 4.** CV curves of the first three cycles for H800 (a), HNP800 (b), HN800 (c), and HNS800 (d) using 1 mol $dm^{-3}$ NaTFSI in DMC:EC (1:1 vol) as electrolyte.

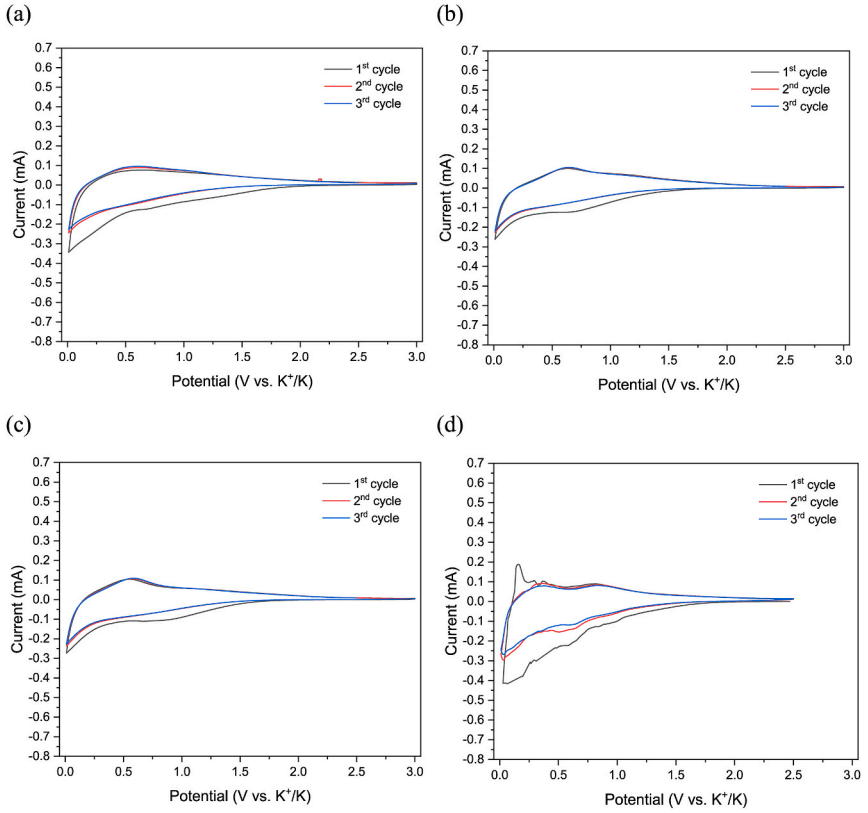


**Fig. 5.** CV curves of the first three cycles for H800 (a), HNP800 (b), HN800 (c), and HNS800 (d) using 0.8 mol $dm^{-3}$ $KPF_6$ in DMC:EC (1:1 in mass) as electrolyte.

N) and interlayer spacing (relative abundance of local domains with greatly expanded interlayer distances, as shown in Fig. 2b), resulting in increased slope and plateau capacities, respectively.

In contrast to the observed behavior for sodium-ion storage, and in line with the CV curves above-discussed, different patterns with lesser contributions from the plateau region can clearly be observed in Fig. 7

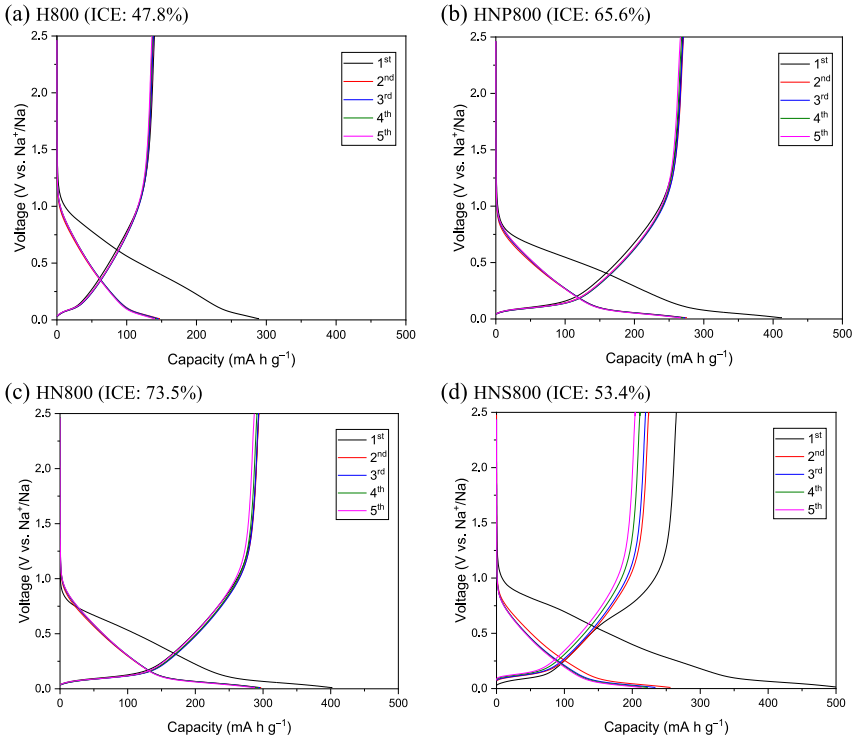


**Fig. 6.** GCD profiles (using three-electrode cells at 0.1 A $g^{-1}$) for H800 (a), HNP800 (b), HN800 (c), and HNS800 (d) using 1 mol $dm^{-3}$ NaTFSI in DMC:EC (1:1 vol) as electrolyte.

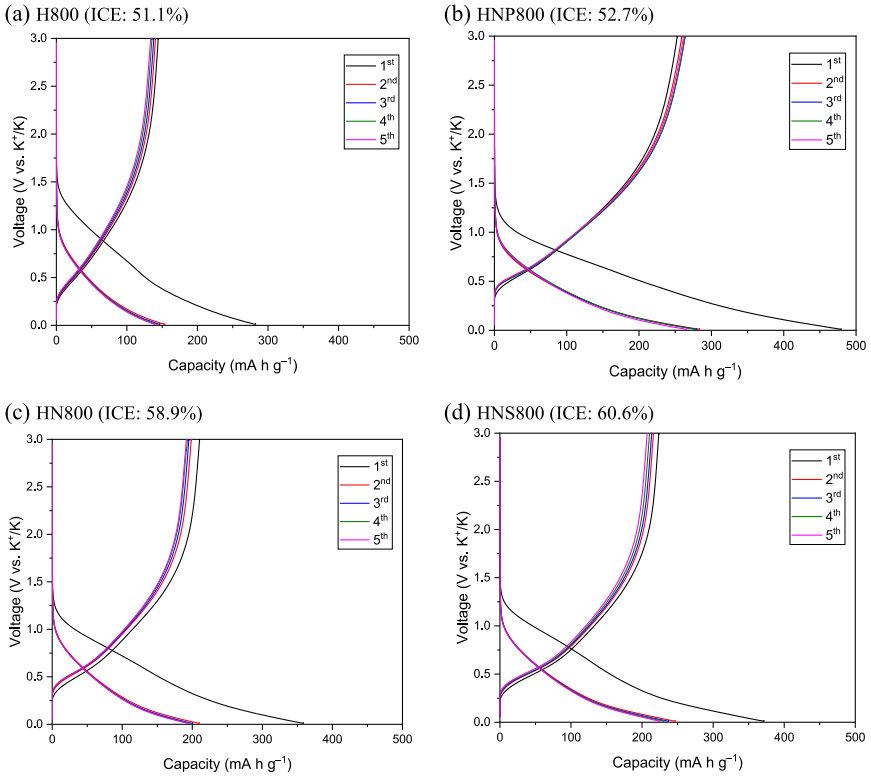


**Fig. 7.** GCD profiles (using three-electrode cells at 0.1 A $g^{-1}$) for H800 (a), HNP800 (b); HN800 (c), and HNS800 (d) using 0.8 mol $dm^{-3}$ $KPF_6$ in DMC:EC (1:1 in mass) as electrolyte.

for potassium-ion half-cells (see also Fig. S12b). In general, relatively low ICE values, in comparison with sodium-ion storage, were obtained (from 51.1 % for H800 to 60.6 % for HNS800). However, these values are considerably better than those reported for hard carbons in some previous studies, which were in the range of 20–50 % [55,56]. Beyond the possible decomposition of the electrolyte, irreversible trapping of $K^+$ ions at oxygen-containing defect sites can explain the low ICE.

Fig. 8 shows the plots of the apparent diffusion coefficients ($D^+_{Na}$ and $D^+_K$), calculated from GITT measurements following the procedure described in a previous work [27]. For sodium-ion diffusion, the profiles shown in Fig. 8a and b clearly reveal an overall slower diffusion rate for HNS800. This result was quite unexpected, since it is generally accepted that S atoms can lead to enlarged interlayer distances and rational adsorption energy values, thereby reducing the ions' diffusion barrier [57]. Furthermore, the diffusion pattern observed for the N-S-doped HC during discharge (i.e., sodiation) notably differed from those observed for the rest of HCs, for which a typical three-stage sequence can be deduced. These stages are the following [58]: (1) at voltages higher than 0.1 V, the observed almost constant and relatively high diffusion rate corresponds to the adsorption of $Na^+$ ions on surface defects, intralayer defects, and the amorphous region; (2) when the voltage is between ca. 0.1 V and 0.05 V, the diffusion coefficient gradually decreased, probably as a consequence of the repulsion between accumulated $Na^+$ ions; and (3) at very low voltages, the gradual increase in $D_{Na^+}$ values can be attributed to the fact that $Na^+$ ions entering micropores or interlayers are reduced, thereby reducing the repulsive forces. The different trend observed for HNS800 clearly indicates a hindered ion mobility across the electrode, which can be explained by the extent of irreversible reactions on surface (especially during the first sodiation). These reactions can lead to intermediate products that may be deposited on the carbon surface, thereby creating a passivation or insulating layer that partly inhibits further ion transport.

To enhance the electrochemical performance of HCs in SIBs, the replacement of ester-based electrolytes with ether-based ones has been proposed [32,59], as latter can form thinner and more stable SEI layers. For PIBs, Wu et al. [50] recently reported an enhanced performance of lignin-derived HCs when KFSI in DEC:EC was used. The authors attributed this improvement to the formation of a KF-rich SEI, which effectively mitigates side reactions and severe structural degradation. Taking into account the potential of these alternative electrolytes, the first five GCD cycles were also acquired for both sodium-ion and potassium-ion half-cells using $NaPF_6$ in DGM and KFSI in DEC:EC, respectively. From the results plotted in Fig. S13 (for $Na^+$ ion), it can be deduced that the use of the DGM-based electrolyte did not lead to a general improvement in performance and only an enhancement in the reversible capacity of the undoped HC was observed. On the contrary, the ICE values were lower than those reported in Fig. 6, except for HNS800, which also exhibited a stable behavior. These findings highlight the extreme complexity of the interactions between the electrolyte and the surface chemistry of HC-based electrodes and suggest that the observed irreversibility is more likely due to undesired reactions between sodium ions and functional groups than to the formation of a thick SEI layer. Concerning the GCD data obtained for $K^+$-ion half-cells (see Fig. S14), the differences in ICE and GCD profiles between both electrolytes were less significant compared to those observed for $Na^+$-ion half-cells. This finding does not appear to be consistent with the data reported in earlier studies [50,60,61], where the use of KFSI salt led to slightly or moderately better ICE, capacity, and stability. Although it is true that further investigation into the effect of the electrolyte is necessary, the results obtained once again demonstrate the complexity of surface chemistry interactions and the difficulty of extrapolating trends to other HC-based electrodes.

The rate capability of WHH-derived HCs is summarized in Fig. 9 (see also Tables S2 and S3 for specific charge capacity values). For sodium ions (Fig. 9a and b), both HN800 and HNP800 also exhibited the best rate capability. At 2 A $g^{-1}$, they maintained notable reversible capacities of 79 and 90 mAh $g^{-1}$ (using NaTFSI in DMC:EC) and 117 and 109 mAh $g^{-1}$ (using $NaPF_6$ in DGM), respectively. The slightly better performance at high current densities observed with diglyme as the electrolyte solvent can be attributed to a reduction in the energy barrier during

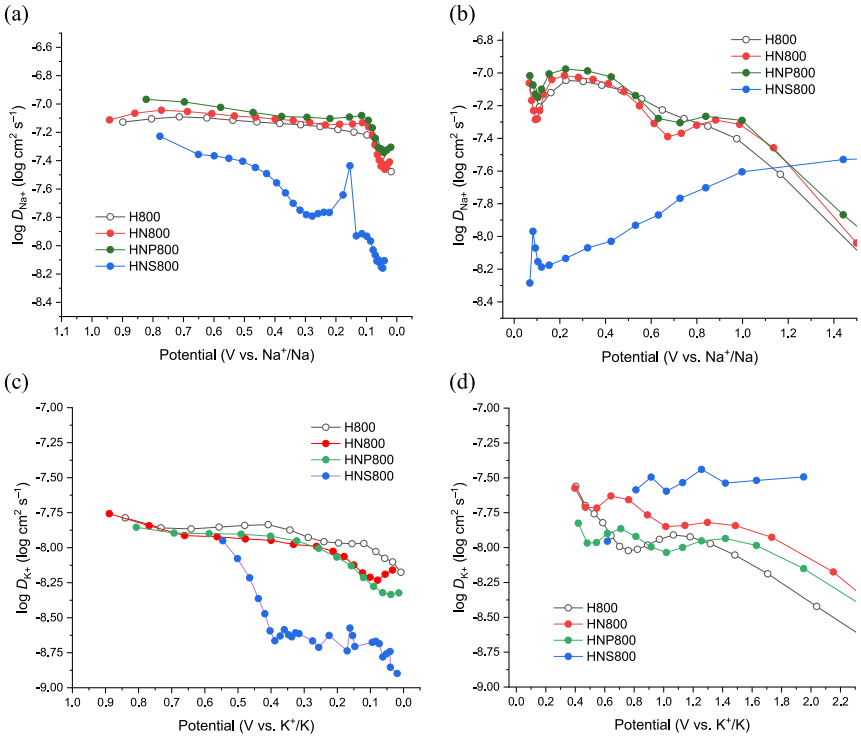


**Fig. 8.** $D_{Na^+}$ values calculated from GITT measurements of WHH-derived carbons (using 1 mol $dm^{-3}$ NaTFSI in DMC:EC as electrolyte) along sodiation (a), and desodiation (b); and $D_{K^+}$ values (using 0.8 mol $dm^{-3}$ $KPF_6$ in DMC:EC as electrolyte) along potassiation (c), and depotassiation (d).

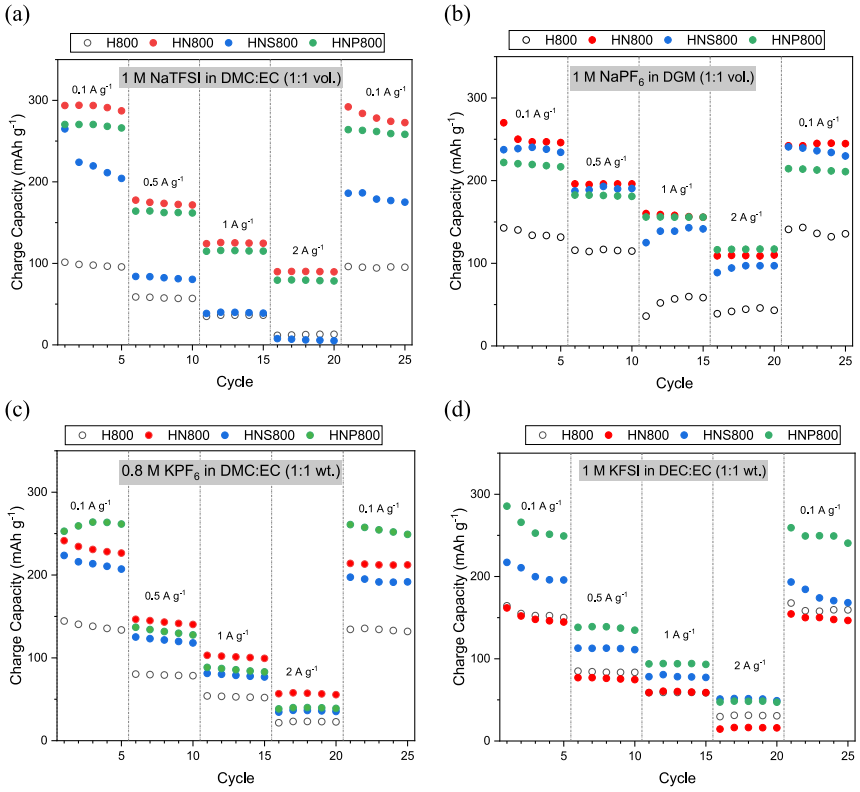


**Fig. 9.** Charge specific capacities at various current densities ranging from 0.1 to 2 A $g^{-1}$ of WHH-derived HCs using NaTFSI in DMC:EC (a) and $NaPF_6$ in DGM (b) in sodium-ion half-cells; and using $KPF_6$ in DMC:EC (c) and KFSI in DEC:EC (d) in potassium-ion half-cells.

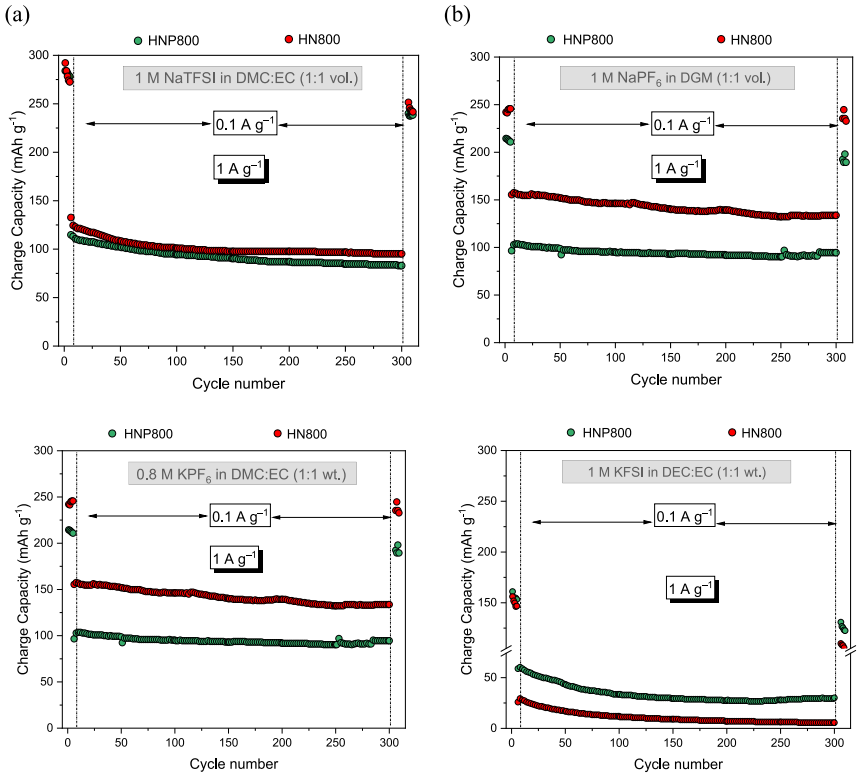


**Fig. 10.** Cycling performance of HNP800 and HN800 at 1 A $g^{-1}$ in sodium-ion half-cells (a,b) and potassium-ion half-cells (c,d).

desolvation at the electrode surface, since it has been reported that the intercalation of $Na^+$-ions into hard carbons is usually accompanied by one molecule of ether (i.e., co-intercalation) [62]. In addition, the improved stability of the HNS800-based anode in DGM was confirmed. In fact, this material exhibited a remarkable electrochemical performance, specially at relatively low current rates. With respect to potassium ions, results plotted in Fig. 9c and d indicate that using KFSI as electrolyte salt did not lead to an improvement of rate capability. Nevertheless, the HC showing the best rate capability was different depending on the electrolyte formulation: HN800 for $KPF_6$ in DMC:EC electrolyte (156 and 117 mAh $g^{-1}$ at 1 and 2 A $g^{-1}$, respectively) and HNP800 (93 mAh $g^{-1}$ at 1 A $g^{-1}$) or HNS800 (49 mAh $g^{-1}$ at 2 A $g^{-1}$) for KFSI in DEC:EC. This fact further demonstrates the importance of the electrode's surface chemistry in the phenomena occurring at the interphase with the electrolyte.

Overall, the HN800 and HNP800 materials demonstrated the best performance as electrodes. To evaluate their cycling stability, 300 discharge-charge cycles were conducted at 1 A $g^{-1}$, following an initial set of five cycles at 0.1 A $g^{-1}$. From Fig. 10, which shows the results obtained for both HCs using all the electrolytes tested here, it can be observed that cycling stability of the single N-doped HC was highly dependent on the electrolyte formulation for both sodium- and potassium-ion half-cells. For sodium ions, the HN800-based electrode in $NaPF_6$/DGM electrolyte showed the best performance and stability, delivering a specific capacity of 134 mAh $g^{-1}$ at cycle 300 and achieving an impressive 99.5 % capacity retention when the current density was returned to 0.1 A $g^{-1}$. This excellent behavior positions this material as highly attractive, considering the mild synthesis conditions (see Table S4 for a comparison of the performance of HN800 with that reported for other heteroatom-doped HCs in the literature).

For potassium-ion half-cells, the HN800 material also exhibited the best performance and stability (36 mAh $g^{-1}$ at cycle 300 and 94.5 % capacity retention) when $KPF_6$ in DMC:EC was used as the electrolyte. However, the cycling stability of HN800 was really poor when KFSI in DEC:EC was employed. Interestingly, the HNP800-based electrode exhibited very similar cycling performances for the two electrolyte formulations tested for either $Na^+$-ion ($NaPF_6$/DGM) or $K^+$-ion ($KPF_6$/DMC:EC) chemistries. Nevertheless, in light of the data reported in Table S5 for other biomass-derived heteroatom-doped HCs, one can conclude that the rate capability and cycling performance of both HN800 and HNP800 materials were relatively modest. This could be explained by the lack of mesopores in the synthesized HCs, as they provide efficient pathways for the rapid intercalation of $K^+$ ions at low voltage. This argument is consistent with findings recently reported by Yuan et al., where the key role of mesopores in $K^+$-ion migration in HCs was highlighted [8]. The authors observed that synthetic HCs with an optimal appropriate mesopore-to-micropore volume ratio (approximately 30:70) exhibited improved rate capability and excellent cycling stability (i.e., 176.6 mAh $g^{-1}$ after 5000 cycles at 2 A $g^{-1}$).

## 4. Conclusions

From the results reported here, we can conclude that WHH-derived hard carbons, produced through a scalable synthesis pathway involving hydrothermal pretreatment with mild heteroatom doping and subsequent thermal annealing at 800 °C, are promising materials for use as anodes in both Na-ion and K-ion batteries. The significant role of both surface chemistry—stemming from intrinsic oxygen-containing and extrinsic heteroatom-containing functional groups—and structural features, particularly interlayer spacing, in influencing the electrochemical properties of HC-based electrodes has been further evidenced. Nevertheless, results also highlight that compatibility with the electrolyte is a key aspect that significantly affects the electrodes performance in terms of ICE, capacity, rate capability, and cycling stability. The excellent rate capability demonstrated by the single N-doped HC for $Na^+$-ion storage with a diglyme-based electrolyte comes at the cost of an unexpected reduction in ICE, decreasing from 73 % in NaTFSI/DMC:EC to 59 % in $NaPF_6$/DGM. Furthermore, the urea-doped HC also showed the best performance for potassium-ion storage in terms of cycling stability at relatively high current rates when $KPF_6$ in DMC:EC was used as the electrolyte. Despite these promising results, the necessity of some level of mesoporosity appears to be required to further enhance its rate capability. The observation that the same material exhibited very poor performance when cycled with a KFSI-based electrolyte confirms the previously-mentioned dependence on the interactions between the electrode and the electrolyte at their interphase. Further research is therefore needed in optimizing the electrolyte formulation.

## CRediT authorship contribution statement

**Daniel Antorán:** Writing – original draft, Methodology, Investigation, Conceptualization. **Darío Alvira:** Methodology, Conceptualization. **Víctor Sebastián:** Methodology, Investigation. **Joan J. Manyà:** Writing – review & editing, Supervision, Funding acquisition, Conceptualization.

## Acknowledgments

This work is part of the research project PID2022-137218OB-I00, funded by MCIN/AEI/10.13039/501100011033 and "ERDF A way of making Europe". VS acknowledges financial support from the research projects PID2021-127847OB-I00 and PDC2022-133866-I00 (MCIN/AEI/10.13039/501100011033), as well as NANBIOSIS and LMA-ELECMI ICTS. The authors also acknowledge the funding from the Aragon Government (Ref. T22_23 R).

## Appendix A. Supplementary data

Supplementary data to this article can be found online at https://doi.org/10.1016/j.biombioe.2025.107633.

## Data availability

Data will be made available on request.

## References

[1] R. Li, Y. Zhou, W. Li, J. Zhu, W. Huang, Structure engineering in biomass-derived carbon materials for electrochemical, Energy Storage, Research (2020) (2020) 1–27, https://doi.org/10.34133/2020/8685436.
[2] F. Yuan, J. Hu, Y. Lei, R. Zhao, C. Gao, H. Wang, B. Li, F. Kang, D. Zhai, Key factor determining the cyclic stability of the graphite anode in potassium-ion batteries, ACS Nano 16 (2022) 12511–12519, https://doi.org/10.1021/acsnano.2c03955.
[3] D. Alvira, D. Antorán, J.J. Manyà, Plant-derived hard carbon as anode for sodium-ion batteries: a comprehensive review to guide interdisciplinary research, Chem. Eng. J. 447 (2022) 137468, https://doi.org/10.1016/j.cej.2022.137468.
[4] L.F. Zhao, Z. Hu, W.H. Lai, Y. Tao, J. Peng, Z.C. Miao, Y.X. Wang, S.L. Chou, H. K. Liu, S.X. Dou, Hard carbon anodes: fundamental understanding and commercial perspectives for Na-ion batteries beyond Li-ion and K-ion counterparts, Adv. Energy Mater. 11 (2021) 1–28, https://doi.org/10.1002/aenm.202002704.
[5] X. Dou, I. Hasa, D. Saurel, C. Vaalma, L. Wu, D. Buchholz, D. Bresser, S. Komaba, S. Passerini, Hard carbons for sodium-ion batteries: structure, analysis, sustainability, and electrochemistry, Mater. Today 23 (2019) 87–104, https://doi.org/10.1016/j.mattod.2018.12.040.
[6] Y. Qin, H. Tang, K. Chang, B. Li, Y. Li, Y. Hou, Z. Chang, In situ synthesis of open hollow tubular MnO/C with high performance anode materials for lithium ion batteries using kapok fiber as carbon matrix, Nanotechnology 30 (2018), https://doi.org/10.1088/1361-6528/aae69e.
[7] S. Alvin, D. Yoon, C. Chandra, H.S. Cahyadi, J.H. Park, W. Chang, K.Y. Chung, J. Kim, Revealing sodium ion storage mechanism in hard carbon, Carbon 145 (2019) 67–81, https://doi.org/10.1016/j.carbon.2018.12.112.
[8] F. Yuan, D. Zhang, Z. Li, H. Sun, Q. Yu, Q. Wang, J. Zhang, Y. Wu, K. Xi, B. Wang, Unraveling the intercorrelation between micro/mesopores and K migration behavior in hard carbon, Small 18 (2022) 1–9, https://doi.org/10.1002/smll.202107113.
[9] Y. Zhu, M. Chen, Q. Li, C. Yuan, C. Wang, A porous biomass-derived anode for high-performance sodium-ion batteries, Carbon 129 (2018) 695–701, https://doi.org/10.1016/j.carbon.2017.12.103.

[10] Y. Li, S. Xu, X. Wu, J. Yu, Y. Wang, Y.S. Hu, H. Li, L. Chen, X. Huang, Amorphous monodispersed hard carbon micro-spherules derived from biomass as a high performance negative electrode material for sodium-ion batteries, J. Mater. Chem. A 3 (2015) 71–77, https://doi.org/10.1039/c4ta05451b.
[11] Y. Li, Y.S. Hu, H. Li, L. Chen, X. Huang, A superior low-cost amorphous carbon anode made from pitch and lignin for sodium-ion batteries, J. Mater. Chem. A 4 (2015) 96–104, https://doi.org/10.1039/c5ta08601a.
[12] Z.L. Yu, S. Xin, Y. You, L. Yu, Y. Lin, D.W. Xu, C. Qiao, Z.H. Huang, N. Yang, S. H. Yu, J.B. Goodenough, Ion-catalyzed synthesis of microporous hard carbon embedded with expanded nanographite for enhanced lithium/sodium storage, J. Am. Chem. Soc. 138 (2016) 14915–14922, https://doi.org/10.1021/jacs.6b06673.
[13] C. Gao, Q. Wang, S. Luo, Z. Wang, Y. Zhang, Y. Liu, A. Hao, R. Guo, High performance potassium-ion battery anode based on biomorphic N-doped carbon derived from walnut septum, J. Power Sources 415 (2019) 165–171, https://doi.org/10.1016/j.jpowsour.2019.01.073.
[14] S. Chen, K. Tang, F. Song, Z. Liu, N. Zhang, S. Lan, X. Xie, Z. Wu, Porous hard carbon spheres derived from biomass for high-performance sodium/potassium-ion batteries, Nanotechnology 33 (2022) 055401, https://doi.org/10.1088/1361-6528/ac317d.
[15] Y. Liu, H. Dai, L. Wu, W. Zhou, L. He, W. Wang, W. Yan, Q. Huang, L. Fu, Y. Wu, A large scalable and low-cost sulfur/nitrogen dual-doped hard carbon as the negative electrode material for high-performance potassium-ion batteries, Adv. Energy Mater. 9 (2019) 1–9, https://doi.org/10.1002/aenm.201901379.
[16] M. Yang, Q. Kong, W. Feng, W. Yao, N/O double-doped biomass hard carbon material realizes fast and stable potassium ion storage, Carbon 176 (2021) 71–82, https://doi.org/10.1016/j.carbon.2021.01.114.
[17] M. Kim, L. Ma, Z. Li, W. Mai, N. Amiralian, A.E. Rowan, Y. Yamauchi, A. Qin, R. A. Afzal, D. Martin, A.K. Nanjundan, J. Li, N and S co-doped nanosheet-like porous carbon derived from sorghum biomass: mechanical nanoarchitecturing for upgraded potassium ion batteries, J. Mater. Chem. A 11 (2023) 16626–16635, https://doi.org/10.1039/d3ta03215a.
[18] X. Ma, N. Xiao, J. Xiao, X. Song, H. Guo, Y. Wang, S. Zhao, Y. Zhong, J. Qiu, Nitrogen and phosphorus dual-doped porous carbons for high-rate potassium ion batteries, Carbon 179 (2021) 33–41, https://doi.org/10.1016/J.CARBON.2021.03.067.
[19] Y. Liu, Y. Qiao, G. Wei, S. Li, Z. Lu, X. Wang, X. Lou, Sodium storage mechanism of N, S co-doped nanoporous carbon: experimental design and theoretical evaluation, Energy Storage Mater. 11 (2018) 274–281, https://doi.org/10.1016/J.ENSM.2017.09.003.
[20] Y. Lu, J. Liang, Y. Hu, Y. Liu, K. Chen, S. Deng, D. Wang, Y. Lu, J. Liang, Y. Hu, Y. Liu, K. Chen, S. Deng, D. Wang, Accurate control multiple active sites of carbonaceous anode for high performance sodium storage: insights into capacitive contribution mechanism, Adv. Energy Mater. 10 (2020) 1903312, https://doi.org/10.1002/AENM.201903312.
[21] J.B.M. Parambath, F. Abla, M. Arooj, A.A. Mohamed, Doping matters in carbon nanomaterial efficiency in environmental remediation, Environ. Sci. Pollut. Res. 30 (2023) 124921–124933, https://doi.org/10.1007/s11356-023-25147-w.
[22] Y. Rangraz, M.M. Heravi, Recent advances in metal-free heteroatom-doped carbon heterogonous catalysts, RSC Adv. 11 (2021) 23725–23778, https://doi.org/10.1039/d1ra03446d.
[23] A. Belcaid, B.H. Beakou, S. Bouhsina, A. Anouar, Biosorption of cobalt and chromium from wastewater using manganese dioxide and iron oxide nanoparticles loaded on cellulose-based biochar: modeling and optimization with machine learning (artificial neural network), Int. J. Biol. Macromol. 282 (2024) 136855, https://doi.org/10.1016/j.ijbiomac.2024.136855.
[24] Hemp production in the EU, (n.d.). https://agriculture.ec.europa.eu/farming/crop-productions-and-plant-based-products/hemp_en#hempproductionintheeu (accessed January 27, 2023).
[25] S.M.Q. Bokhari, K. Chi, J.M. Catchmark, Structural and physico-chemical characterization of industrial hemp hurd: impacts of chemical pretreatments and mechanical refining, Ind. Crops Prod. 171 (2021) 113818, https://doi.org/10.1016/J.INDCROP.2021.113818.
[26] H. Wang, W. Yu, N. Mao, J. Shi, W. Liu, Effect of surface modification on high-surface-area carbon nanosheets anode in sodium ion battery, Microporous Mesoporous Mater. 227 (2016) 1–8, https://doi.org/10.1016/j.micromeso.2016.02.003.
[27] D. Antorán, D. Alvira, M.E. Peker, H. Malón, S. Irusta, V. Sebastián, J.J. Manyà, Waste hemp hurd as a sustainable precursor for affordable and high-rate hard carbon-based anodes in sodium-ion batteries, Energy Fuels 37 (2023) 9650–9661, https://doi.org/10.1021/acs.energyfuels.3c01040.
[28] D. Antorán, D. Alvira, V. Sebastián, J.J. Manyà, Enhancing waste hemp hurd-derived anodes for sodium-ion batteries through hydrochloric acid-mediated hydrothermal pretreatment, Biomass Bioenergy 184 (2024) 107197, https://doi.org/10.1016/j.biombioe.2024.107197.
[29] P. Wang, Z. Gong, D. Wang, R. Hu, K. Ye, Y. Gao, K. Zhu, J. Yan, G. Wang, D. Cao, Facile fabrication of F-doped biomass carbon as high-performance anode material for potassium-ion batteries, Electrochim. Acta 389 (2021), https://doi.org/10.1016/j.electacta.2021.138799.
[30] D. Alvira, D. Antorán, J.J. Manyà, Assembly and electrochemical testing of renewable carbon-based anodes in SIBs: a practical guide, J. Energy Chem. 75 (2022) 457–477, https://doi.org/10.1016/j.jechem.2022.09.002.
[31] A. Sadezky, H. Muckenhuber, H. Grothe, R. Niessner, U. Pöschl, Raman microspectroscopy of soot and related carbonaceous materials: spectral analysis and structural information, Carbon 43 (2005) 1731–1742, https://doi.org/10.1016/j.carbon.2005.02.018.
[32] D. Alvira, D. Antorán, H. Darjazi, G.A. Elia, V. Sebastian, J.J. Manyà, Sustainable conversion of vine shoots and pig manure into high-performance anode materials for sodium-ion batteries, J. Power Sources 614 (2024), https://doi.org/10.1016/j.jpowsour.2024.235043.
[33] J. Liao, H. Qiu, P. Zhou, J. Chen, J. Xue, X. Zhao, J. Nan, Unraveling the effect of the microstructure of agricultural waste plants-derived hard carbons on the sodium storage performance, Fuel 376 (2024) 132664, https://doi.org/10.1016/J.FUEL.2024.132664.
[34] J. Liang, H. Lin, C. Li, L. Zhang, S. Zhang, S. Wang, J. Xiang, S. Hu, Y. Wang, X. Hu, Interaction of derivatives of cellulose and lignin in co-HTC, co-pyrolysis and co-activation, Fuel 351 (2023) 129033, https://doi.org/10.1016/J.FUEL.2023.129033.
[35] Y. Li, Y. Lu, Q. Meng, A.C.S. Jensen, Q. Zhang, Q. Zhang, Y. Tong, Y. Qi, L. Gu, M. M. Titirici, Y.S. Hu, Regulating pore structure of hierarchical porous waste cork-derived hard carbon anode for enhanced Na storage performance, Adv. Energy Mater. 9 (2019), https://doi.org/10.1002/aenm.201902852.
[36] C. Cai, Y. Chen, P. Hu, T. Zhu, X. Li, Q. Yu, L. Zhou, X. Yang, L. Mai, Regulating the interlayer spacings of hard carbon nanofibers enables enhanced pore filling sodium storage, Small 18 (2022) 1–8, https://doi.org/10.1002/smll.202105303.
[37] F. Zheng, K. Chu, Y. Yang, Z. Li, L. Wei, Y. Xu, G. Yao, Q. Chen, Optimizing the interlayer spacing of heteroatom-doped carbon nanofibers toward ultrahigh potassium-storage performances, ACS Appl. Mater. Interfaces 14 (2022) 9212–9221, https://doi.org/10.1021/ACSAMI.1C24275.
[38] X. Chang, X. Zhou, X. Ou, C.S. Lee, J. Zhou, Y. Tang, Ultrahigh nitrogen doping of carbon nanosheets for high capacity and long cycling potassium ion storage, Adv. Energy Mater. 9 (2019) 1902672, https://doi.org/10.1002/AENM.201902672.
[39] Z. Xu, J. Wang, Z. Guo, F. Xie, H. Liu, H. Yadegari, M. Tebyetekerwa, M.P. Ryan, Y. S. Hu, M.M. Titirici, The role of hydrothermal carbonization in sustainable sodium-ion battery anodes, Adv. Energy Mater. 12 (2022) 2200208, https://doi.org/10.1002/aenm.202200208.
[40] X. Shi, Y. Chen, Y. Lai, K. Zhang, J. Li, Z. Zhang, Metal organic frameworks templated sulfur-doped mesoporous carbons as anode materials for advanced sodium ion batteries, Carbon 123 (2017) 250–258, https://doi.org/10.1016/J.CARBON.2017.07.056.
[41] S. Alvin, C. Chandra, J. Kim, Extended plateau capacity of phosphorus-doped hard carbon used as an anode in Na- and K-ion batteries, Chem. Eng. J. 391 (2020) 123576, https://doi.org/10.1016/j.cej.2019.123576.
[42] M. Smith, L. Scudiero, J. Espinal, J.S. McEwen, M. Garcia-Perez, Improving the deconvolution and interpretation of XPS spectra from chars by ab initio calculations, Carbon 110 (2016) 155–171, https://doi.org/10.1016/J.CARBON.2016.09.012.
[43] C. Chen, Y. Huang, Y. Zhu, Z. Zhang, Z. Guang, Z. Meng, P. Liu, Nonignorable influence of oxygen in hard carbon for sodium ion storage, ACS Sustain. Chem. Eng. 8 (2020) 1497–1506, https://doi.org/10.1021/acssuschemeng.9b05948.
[44] J.H. Zhou, Z.J. Sui, J. Zhu, P. Li, D. Chen, Y.C. Dai, W.K. Yuan, Characterization of surface oxygen complexes on carbon nanofibers by TPD, XPS and FT-IR, Carbon 45 (2007) 785–796, https://doi.org/10.1016/J.CARBON.2006.11.019.
[45] Z. Liu, S. Wu, Y. Song, T. Yang, Z. Ma, X. Tian, Z. Liu, Non-negligible influence of oxygen in hard carbon as an anode material for potassium-ion batteries, ACS Appl. Mater. Interfaces 14 (2022) 47674–47684, https://doi.org/10.1021/acsami.2c12390.
[46] X. Feng, Y. Bai, L. Zheng, M. Liu, Y. Li, R. Zhao, Y. Li, C. Wu, Effect of different nitrogen configurations on sodium storage properties of carbon anodes for sodium ion batteries, ACS Appl. Mater. Interfaces 13 (2021) 56285–56295, https://doi.org/10.1021/ACSAMI.1C18464.
[47] Y. Xie, Y. Chen, L. Liu, P. Tao, M. Fan, N. Xu, X. Shen, C. Yan, Y. Xie, Y. Chen, L. Liu, P. Tao, M. Fan, N. Xu, X. Shen, C. Yan, Ultra-high pyridinic N-doped porous carbon monolith enabling high-capacity K-ion battery anodes for both half-cell and full-cell applications, Adv. Mater. 29 (2017) 1702268, https://doi.org/10.1002/ADMA.201702268.
[48] C. Chen, M. Wu, J. Liu, Z. Xu, K. Zaghib, Y. Wang, Effects of ester-based electrolyte composition and salt concentration on the Na-storage stability of hard carbon anodes, J. Power Sources 471 (2020) 228455, https://doi.org/10.1016/j.jpowsour.2020.228455.
[49] H. Fang, S. Gao, M. Ren, Y. Huang, F. Cheng, J. Chen, F. Li, Dual-function presodiation with sodium diphenyl ketone towards ultra-stable hard carbon anodes for sodium-ion batteries, Angew. Chem., Int. Ed. 62 (2023) 1–5, https://doi.org/10.1002/anie.202214717.
[50] Z. Wu, J. Zou, S. Shabanian, K. Golovin, J. Liu, The roles of electrolyte chemistry in hard carbon anode for potassium-ion batteries, Chem. Eng. J. 427 (2022) 130972, https://doi.org/10.1016/j.cej.2021.130972.
[51] L. Xiao, Y. Cao, W.A. Henderson, M.L. Sushko, Y. Shao, J. Xiao, W. Wang, M. H. Engelhard, Z. Nie, J. Liu, Hard carbon nanoparticles as high-capacity, high-stability anodic materials for Na-ion batteries, Nano Energy 19 (2016) 279–288, https://doi.org/10.1016/J.NANOEN.2015.10.034.
[52] E.M. Lotfabad, J. Ding, K. Cui, A. Kohandehghan, W.P. Kalisvaart, M. Hazelton, D. Mitlin, High-density sodium and lithium ion battery anodes from banana peels, ACS Nano 8 (2014) 7115–7129, https://doi.org/10.1021/nn502045y.
[53] T. Zhang, J. Mao, X. Liu, M. Xuan, K. Bi, X.L. Zhang, J. Hu, J. Fan, S. Chen, G. Shao, Pinecone biomass-derived hard carbon anodes for high-performance sodium-ion batteries, RSC Adv. 7 (2017) 41504–41511, https://doi.org/10.1039/c7ra07231g.
[54] Y. Qian, Y. Li, Z. Yi, J. Zhou, Z. Pan, J. Tian, Y. Wang, S. Sun, N. Lin, Y. Qian, Revealing the double-edged behaviors of heteroatom sulfur in carbonaceous materials for balancing K-storage capacity and stability, Adv. Funct. Mater. 31 (2021) 2006875, https://doi.org/10.1002/ADFM.202006875.

[55] R. Hao, H. Lan, C. Kuang, H. Wang, L. Guo, Superior potassium storage in chitin-derived natural nitrogen-doped carbon nanofibers, Carbon N Y 128 (2018) 224–230, https://doi.org/10.1016/j.carbon.2017.11.064.
[56] S. Tao, W. Xu, J. Zheng, F. Kong, P. Cui, D. Wu, B. Qian, S. Chen, L. Song, Soybean roots-derived N, P Co-doped mesoporous hard carbon for boosting sodium and potassium-ion batteries, Carbon 178 (2021) 233–242, https://doi.org/10.1016/J.CARBON.2021.03.022.
[57] B. Sun, Q. Zhang, W. Xu, R. Zhao, C. Zhang, J. Guo, H. Zhu, G. Yuan, W. Lv, X. Li, N. Yang, Edge-enriched and S-doped carbon nanorods to accelerate electrochemical kinetics of sodium/potassium storage, Carbon 201 (2023) 776–784, https://doi.org/10.1016/J.CARBON.2022.09.066.
[58] X. Feng, Y. Li, Y. Li, M. Liu, L. Zheng, Y. Gong, R. Zhang, F. Wu, C. Wu, Y. Bai, Unlocking the local structure of hard carbon to grasp sodium-ion diffusion behavior for advanced sodium-ion batteries, Energy Environ. Sci. 17 (2024) 1387–1396, https://doi.org/10.1039/D3EE03347C.
[59] Y. Li, F. Wu, Y. Li, M. Liu, X. Feng, Y. Bai, C. Wu, Ether-based electrolytes for sodium ion batteries, Chem. Soc. Rev. 51 (2022) 4484–4536, https://doi.org/10.1039/D1CS00948F.
[60] L. Larbi, B. Larhrib, A. Beda, L. Madec, L. Monconduit, C. Matei Ghimbeu, Impact of hard carbon properties on their performance in potassium-ion batteries, ACS Appl. Energy Mater. 6 (2023) 5274–5289, https://doi.org/10.1021/ACSAEM.3C00201/ASSET/IMAGES/LARGE/AE3C00201_0008.JPEG.
[61] Y. Peng, W. Zhou, Z. Wang, H. Liu, Q. Fu, K. Xiao, J. Wu, Z. Wang, J. Tu, P. Gao, J. Liu, Regulating anion chemistry with F-containing bonds enable superior potassium ions storage in hard carbon, Energy Storage Mater. 62 (2023) 102942, https://doi.org/10.1016/J.ENSM.2023.102942.
[62] J. Pan, Y.Y. Sun, Y. Yan, L. Feng, Y. Zhang, A. Lin, F. Huang, J. Yang, Revisit electrolyte chemistry of hard carbon in ether for Na storage, JACS Au 1 (2021) 1208–1216, https://doi.org/10.1021/jacsau.1c00158.